Optimizing Ni–Fe–Ga alloys into Ni_2FeGa for the Hydrogenation of CO_2 into Methanol

Thomas E. L. Smitshuysen,[a] Monia R. Nielsen,[b] Tim Pruessmann,[c] Anna Zimina,[c] Thomas L. Sheppard,[c, d] Jan-Dierk Grunwaldt,[c, d] Ib Chorkendorff,[a] and Christian D. Damsgaard*[a, b]

A screening study of the catalytic performance of ternary alloy nanoparticles containing nickel, iron and gallium supported on silica for methanol synthesis from CO_2 and H_2 was performed. Catalysts were prepared by incipient wetness impregnation and subsequently reduced in H_2 before catalytic testing. Ni_2FeGa showed the best performance of the tested catalysts in terms of methanol yield. An optimization of the preparation was done to improve activity and selectivity, reaching a performance close to that of commercially available $Cu/ZnO/Al_2O_3/MgO$ at low reaction temperatures and pressure. Extensive in situ characterisation using environmental TEM, in situ XRD and in situ EXAFS of the formation of the Ni_2FeGa catalyst explains an optimal reduction temperature of 550 °C: warm enough that the three atomic species will form an alloy while cold enough to prevent the catalyst from sintering during the formation.

Introduction

Human energy consumption is both a current and urgent issue, due to its direct relation towards increased financial needs and the impact on nature as a whole, for example the current prevalence of fossil-based carbon feedstock being an anthropogenic source of global warming. The present problem of having an energy infrastructure mainly running on carbon-fuels could be mitigated by utilizing the emitted CO_2 for synthesizing fuels, thus having a closed sustainable loop of combustion and recycling. *The methanol economy* presents such a scenario, where CO_2 from point-sources in the short term and air-capture in future endeavours is reacted with H_2 to create methanol.[1–4] Having H_2 produced from renewable electricity by electrolysis makes this fuel feedstock sustainable. The bulk chemical of methanol is a resource used both as a combustion fuel or additive to gasoline and more importantly as a feedstock for synthesizing other products such as formaldehyde, dimethyl ether, acetic acid and olefins.[5] The commercial production of methanol uses syngas reacted over $Cu/ZnO/Al_2O_3$,[6–9] where the syngas consisting of a mixture of H_2, CO_2 and CO is mostly supplied from steam reforming of natural gas or gasification of coal. This methanol catalyst system has been highly optimized through the last century with typical working conditions around 200–300 °C and 50–100 bar pressure, but with the drawback that sintering of Cu nanoparticles reduces their activity over time.[10,11] Furthermore CO in the feed-gas is necessary to thermodynamically hinder the production of water from CO_2 through the reverse water gas shift reaction (rWGS) which inhibits the methanol synthesis.[9,12] The desire to use mainly CO_2 as a carbon-source therefor requires new catalysts that are able to suppress the rWGS by higher selectivity. Given the potential of methanol as a sustainable energy carrier on a global scale[1–3] and the need for utilizing delocalized production in more rural and underdeveloped regions, there is a desire to develop novel catalysts that work sufficiently at lower pressure and temperature than the current large methanol plants and with sufficient selectivity and resistance to sintering.

A development from the well-established Cu/ZnO is the use of post-transition metals such as gallium and indium. Even though these materials are much more costly than Cu and Zn, they behave differently to their industrial counter-part making them interesting for research into novel catalysts. One rather unconventional reaction mechanism discovered is the active site formed by producing water, leaving oxygen vacancies in In_2O_3, which gets remedied by CO_2 bonding and formation of methanol since the reaction-pathway for forming CO is not energetically favoured.[13,14] Experimental work showed that In_2O_3 is very selective and stability-wise outperforms $Cu/ZnO/Al_2O_3$, when reacting CO_2 and H_2 in 1:4 at 300 °C and 5 MPa.[15,16] Improvement of this catalyst has been achieved through doping of metals e.g. Pd.[17–19] Also reported is the use of Ga_2O_3/Pd by Fujitani et al. which at the time competed well with the

[a] *T. E. L. Smitshuysen, Prof. I. Chorkendorff, Prof. C. D. Damsgaard*
Surfcat, Department of Physics
Technical University of Denmark
Fysikvej, Building 311
DK-2800 Lyngby (Denmark)
E-mail: cdda@dtu.dk
[b] *Dr. M. R. Nielsen, Prof. C. D. Damsgaard*
DTU Nanolab
Technical University of Denmark
Fysikvej, Building 307
DK-2800 Lyngby (Denmark)
[c] *Dr. T. Pruessmann, Dr. A. Zimina, Dr. T. L. Sheppard, Prof. J.-D. Grunwaldt*
Institute for Chemical Technology and Polymer Chemistry
Karlsruhe Institute of Technology
Engesserstr. 20
D-76131 Karlsruhe (Germany)
[d] *Dr. T. L. Sheppard, Prof. J.-D. Grunwaldt*
Institute of Catalysis Research and Technology
Karlsruhe Institute of Technology
Hermann-von-Helmholtz Platz 1
76344 Eggenstein-Leopoldshafen (Germany)

Cu/ZnO based catalyst.[20] For the renowned $Cu/ZnO/Al_2O_3$, Ga_2O_3 has been used as a structural promoter for dispersing the copper,[21] but also actively promoting the reaction.[22–24] Medina et al. investigated Cu Ga supported on silica, where it was found that gallium improved the methanol selectivity and the intrinsic activity of Cu.[24] They found using *in situ* DRIFTS that formate species were adsorbed on Ga_2O_3 and suggested that Ga_2O_3 promoted the formation of methanol by adsorbing carbon-species and using H_2 migrating from metallic copper.

Apart from using solid oxides, forming intermetallics of transition metals with gallium or indium as very active catalysts has been achieved with good results in the last decade. Well-known methanation and Fischer-Tropsch catalysts have been adjusted this way towards making methanol. Most notably is the Pd_2Ga[25–28] that has been reported as a very active methanol catalyst with an intrinsic activity at least double that of $Cu/ZnO/Al_2O_3$.[26] Pd-based intermetallics such as Pd_2Ga[29] and PdZn[30] have also shown able to perform the syngas-to-dimethyl ether reaction with notable activity and doing so more selectively and stable than Cu/Zn. Pd In and Ni In alloys has also been synthesized,[31,32] where the similar Pd_2In proved most active but the In_2Pd was much more selective, explained by the fact that the indium is partly oxidized in the In_2Pd-alloy.[32] Furthermore Co Ga[33] and Ni Ga[34–36] catalysts have been discovered based on determination and optimizing of the rate-limiting reaction step based on work done by Grabow et al. on the Cu(111) facet.[37] Especially the Ni_5Ga_3 has been found to be the most active, but the catalyst struggles through deactivation by coking.[35]

Given the previous success of making active catalysts for methanol synthesis using alloys composed of gallium together with other transition metals, the research presented in this article will evolve around the compositional phase-space of Ni Fe Ga. Recent papers showing ternary alloys for hydrogenation of alkynes[38,39] inspired the screening of $Ni_xFe_yGa_z$ for methanol synthesis presented in this article, especially the Heusler alloys[40,41] which are a frequent intermetallic crystalline phase for ternary transition metal alloys.

In this work a screening consisting of five different $Ni_xFe_yGa_z/SiO_2$ has resulted in an active Ni_2FeGa/SiO_2 catalyst. Afterwards this catalyst has been optimized in its synthesis procedure and studied using *in situ* characterisation methods. The final catalyst is one that selectively produce methanol at 160–200 °C and is stable for 100+ hours at 190 °C. At high temperatures beyond 200 °C it suffers from lower selectivity and activity compared to commercially supplied $Cu/ZnO/Al_2O_3/MgO$.

Results and Discussion

Ni Fe Ga/SiO_2 survey study

Catalytic performance of the Ni Fe Ga/SiO_2 catalysts. In order to find an optimized composition of Ni Fe Ga/SiO_2, five different catalysts with variable Ni:Fe:Ga concentrations were prepared for the methanol synthesis reaction, all reduced at 800 °C for eight hours in H_2 directly before running the reaction. The starting point was taken from the Heusler intermetallic of Ni_2FeGa (expected nominal composition), which has been produced as supported nanoparticles before,[42] and making different catalysts with increasing amount of gallium in them, and so $Ni_{1.7}FeGa_{1.3}$ and $NiFeGa_2$ were also tested. Additionally the binary alloys of NiFe and FeGa were tested: NiFe since it was desired to try a catalyst in the setup that did not contain gallium even though Ni Fe alloys have already been reported[43] and FeGa because Fe Ga alloys have to our knowledge not been published for any catalytic reaction. Testing the catalytic activity of pure iron and nickel were not performed, as they are well known hydrocarbon-catalysts.[44–46] In Figure 1 the yield of methanol and selectivity are shown recorded at different temperatures.

Regarding the activity of the tested catalyst, the stoichiometric Heusler Ni_2FeGa reached the highest methanol rate, though compared to $Cu/ZnO/Al_2O_3/MgO$ under similar conditions in Figure 3, it have only one third of the activity. Increasing the content of gallium reduced the rate of methanol formation but increased the selectivity to methanol. With the lowest methanol rates and selectivities are NiFe and FeGa: NiFe because it produced much more CO and methane as shown in Figure S2 of the supplementary; FeGa surprisingly did not produce any measurable quantity of gaseous products in the

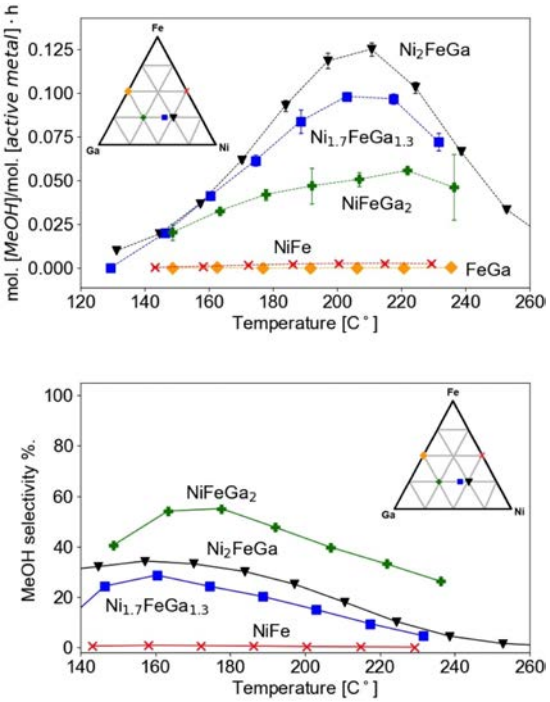

Figure 1. Top, the methanol yield per mole of Ni, Fe and Ga. **Bottom**, the methanol selectivity of the tested Ni Fe Ga/SiO_2. The noted composition is the expected nominal composition. FeGa is neglected from the selectivity because it did not produce a measurable amount of any detected gasses. Reaction conditions: 1.2 bar, 100 ml/min of CO_2/H_2 in 1:3, GHSV of 8000 h^{-1} and a GHSV per weight of 130 000 $N cm^3 h^{-1} g_{NiFeGa}^{-1}$. Detected by-products are CO, CH_4 and C_2H_6 and concentrations of these are shown in Figure S2 in the supplementary. Dimethyl ether was not measured beyond the detection limit. Uncertainties are estimated by propagation of error.

Table 1. Collection of results for the different catalysts in the survey-study, including EDX spectroscopy and particle diameter estimated with ex situ TEM and ex situ XRD. The nominal composition is based on the weighted pre-cursor nitrate-salts. Values in parenthesis denote the standard deviation on the last digit based on the sample collection.

Target	Nominal	EDX Pre-test	EDX Post-test	TEM D(σ) [nm]
Ni_2FeGa	$Ni_{2.01}Fe_{0.99}Ga$	$Ni_{2.02(5)}Fe_{1.00(5)}Ga_{0.98(4)}$	$Ni_{2.00(10)}Fe_{0.98(9)}Ga_{0.93(5)}$	7.4(3.7)
$Ni_{1.7}FeGa_{1.3}$	$Ni_{1.67}Fe_{1.03}Ga_{1.3}$	$Ni_{1.68(3)}Fe_{1.02(4)}Ga_{1.30(4)}$	$Ni_{1.67(3)}Fe_{1.03(3)}Ga_{1.30(3)}$	5.6(1.5)
$NiFeGa_2$	$Ni0_{.99}Fe_{1.01}Ga_2$	$Ni_{1.04(5)}Fe_{1.02(5)}Ga_{1.94(5)}$	$Ni_{0.97(5)}Fe_{1.09(6}Ga_{1.94(6)}$	6.0(2.6)
NiFe	$Ni_{2.01}Fe_{1.99}$	$Ni_{2.02(7)}Fe_{1.98(9)}$	$Ni_{2.02(7)}Fe_{1.98(7)}$	8.0(3.4)
FeGa	$Fe_{1.99}Ga_{2.01}$	$Fe_{2.02(5)}$ $Ga_{1.98(5)}$	$Fe_{2.12(3)}$ $Ga_{1.88(3)}$	9.2(3.2)

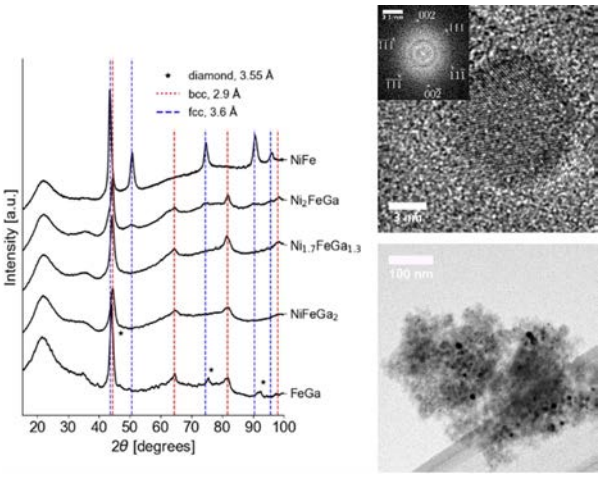

Figure 2. Left, XRD of the tested Ni Fe Ga/SiO_2 catalysts acquired after catalytic reaction. Lines denote reference-patterns of a face centred cubic lattice and a body centred cubic lattice, with a cubic unit-cell length of 3.6 Å and 2.9 Å. Stars denote a crystal-structure of diamond with lattice-length 3.55 Å. X-ray source was a Cu Kα with wavelength 1.5418 Å. **Top right**, High resolution TEM of Ni_2FeGa/SiO_2 with Fourier transform denoting fcc crystal-planes. **Bottom right**, bright field TEM of Ni_2FeGa/SiO_2.

tested temperature-range. Especially because as mentioned earlier gallium alloyed with Co, Ni, Cu and Pd has been reported catalytically active, thus the state of FeGa tested in this work must be vastly different.

Besides the different activities, all the catalyst behaved in the same manner, showing decreased methanol formation rate at elevated temperatures, which is due to the increased CO production inhibiting the methanol equilibrium through the production of water by rWGS. All catalysts showed optimum methanol yield at temperatures around 210 °C though this optimum is readily controlled by the gas velocity.

Crystalline phase and chemical composition of Ni Fe Ga catalysts. To support the activity experiments, characterization of the catalysts was done *ex situ* to the activity experiments using XRD, TEM and SEM-EDX. Table 1 shows the macroscopic composition of Ni, Fe and Ga normalised to a Heusler stoichiometry (sum of four). Here it is apparent that within a standard deviation, the expected nominal and measured composition prior and after catalytic experiments are the same, except for the FeGa where prior and post composition differs little from a single standard deviation. Therefore the different catalysts will be referred to with their nominal composition.

Presented in Figure 2 are XRD-patterns of all the respective alloys alongside TEM images showing the Ni_2FeGa nanoparticles supported on silica. Supporting the XRD patterns are reference lines for face centred (3.6 Å) and body centred (2.9 Å) cubic crystal -structures showing that in all cases these two structures explain the diffraction peaks, except for FeGa. FeGa has additional peaks that fit with a diamond crystal-structure. The transition between the fcc and bcc structures go from NiFe with a very clear fcc structure to a bcc when adding more gallium to the alloy. In the case of the most active alloy Ni_2FeGa, clear trends of both fcc and bcc are present, showing both individual peaks and as a shoulder on the most intense peak at a 2θ-angle of 44°. Taken that Ni, Fe and Ga are close in the periodic table and the scattering cross-section of X-rays is proportional to the second power of the atomic charge, intermetallic structures are hard to distinguished from random alloyed structures, but the size of the crystalline unit-cell corresponds very well to a Heusler crystal in the bcc case and a tetragonal Heusler or γ-Heusler in the fcc case. As no long-range intermetallic ordering has been observed, the alloyed crystal structures will be noted as bcc and fcc as well.

The acquired HR-TEM images shown in Figure 2, top right, and Figure 2s in the supplementary information show that the crystalline phase of the nanoparticles to be the fcc structure, but the difference between {111}-planes of fcc and {110}-planes of bcc is less than 0.02 Å making them indistinguishable. Alloyed Ni_2FeGa nanoparticles are not expected to be phase-pure since Ni_2FeGa is known for being difficult to synthesize in a pure single crystal phase.[42] Figure S3.0 of the supplementary shows two HR-TEM images, where two different crystal phases are visible within the sample nanoparticle. Even in the case where an intermetallic long-range order is achieved of either Heusler or tetragonal Heusler, Ni_2FeGa has been shown to be able to undergo the martensitic transformation similarly that of iron going continuously from a bcc to an fcc structure, both for alloyed ribbons and for large single crystals.[47–50] Therefore it is likely that Ni Fe Ga alloyed nanoparticles individually pick between fcc and bcc phases dependent on small fluctuations in the local atomic environment or the chemical composition of the three components. The compositions were found to fluctuate from nanoparticle to nanoparticle, as *ex situ* STEM-EDX and STEM-EELS of Ni_2FeGa shows, Table S2 in the supplementary. This observation also substantiates the claim that ternary-alloyed nanoparticles have been made.

BF-TEM images like the one shown in Figure 2, bottom right, were acquired for all the tested catalysts, exemplified in Figure S4 in the supplementary information. Size distributions based on BF-TEM in Table 1 show a trend, where more gallium-rich alloys produce smaller nanoparticles. FeGa and NiFe have on average 2.6 nm larger nanoparticles than the gallium-containing ternary alloys. For the ternary alloys the resulting nanoparticles are smaller, where the largest particles from

Ni_2FeGa are also the ones with the highest methanol yield. Thus the difference in activity towards making methanol is not explained by difference in surface areas.

In part conclusion, addition of gallium has changed the selectivity of Ni Fe catalysts from methane towards methanol. Furthermore the survey has shown that there is an optimum of gallium content for improving the activity, but this can be done only at the expense of selectivity.

Optimization of Ni_2FeGa/SiO_2

Catalytic performance of the Ni Fe Ga/SiO_2 catalysts. Following the screening-study, the most active catalyst i.e. Ni_2FeGa/SiO_2 was optimized further in terms of reduction temperature. 800 °C in high concentrations of H_2 for eight hours was initially chosen based on literature.[38,39,42] Therefore samples of Ni_2FeGa/SiO_2 were prepared by 4 hours of reduction at 300 °C, 400 °C, 500 °C, 550 °C, 600 °C and 700 °C respectively, after which they were all tested for their catalytic activity. Figure 3 shows the outcome in terms of methanol yield and selectivity both in terms of reduction temperature and compared to our prepared sample of the commercially available $Cu/ZnO/Al_2O_3/MgO$.

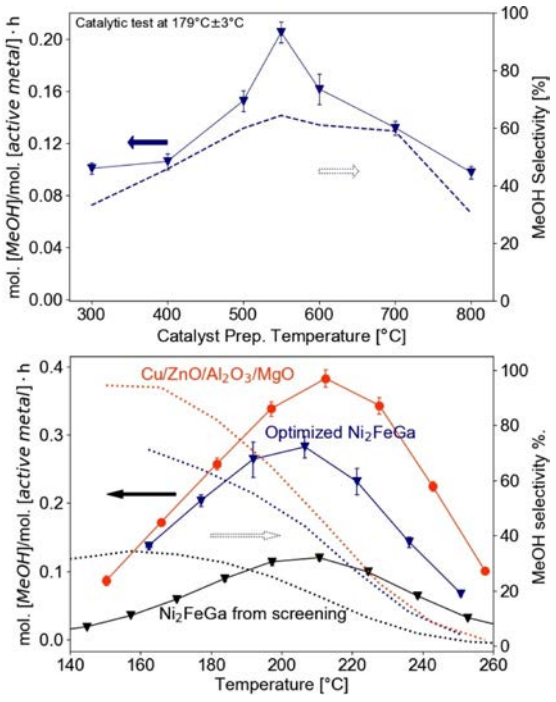

Figure 3. Top, the yield of methanol per mole of active metal (Ni, Fe and Ga) of Ni_2FeGa/SiO_2 and selectivity recorded at 179 °C, versus the reduction temperature used in preparation of the catalyst. All points on the plot show individual test of Ni_2FeGa/SiO_2, all reduced in 90% H_2/Ar for 4 hours prior to the activity experiment, except for the 800 °C-sample that was reduced for 8 hours. Catalysts were all tested at different temperatures, which is shown in Figure S6 in the supplementary information. **Bottom**, the yield of methanol per mole of active metal (Ni, Fe, Ga, Cu) and selectivity versus the reaction temperature, for $Cu/ZnO/Al_2O_3/MgO$ and Ni_2FeGa/SiO_2 both reduced at 550 °C and 800 °C. Reaction conditions: 1.2 bar, 100 ml/min of CO_2/H_2 in 1:3, GHSV of 8000 h^{-1} and a GHSV per weight of 130000 $N cm^3 h^{-1} g_{NiFeGa}^{-1}$ or $N cm^3 h^{-1} g_{Cu}^{-1}$.

A clear optimum in catalytic performance is found when the Ni_2FeGa/SiO_2 has been reduced at 550 °C for 4 hours, both in terms of methanol yield and selectivity, where both values are increased two-fold compared to the sample reduced at 800 °C for 8 hours. As Figure 3 Top clearly shows there is an increase and decrease in both methanol yield and selectivity around the reduction temperature of 550 °C, showing that two different formation processes must take place at low and high reduction temperatures. Ni_2FeGa reduced at 550 °C performs similarly at low temperature as the $Cu/ZnO/Al_2O_3/MgO$ but is outperformed at higher temperatures as Figure 3 bottom shows. In literature the most similar catalyst would be Ni_5Ga_3/SiO_2 reported by Studt et al., which is similar in activity compared to Cu/ZnO[34] and thus also more active than Ni_2FeGa. The obtained activity of Ni_2FeGa in this work is achieved with lower gallium content and with a 150 °C decrease in reduction temperature compared to Ni_5Ga_3/SiO_2 as it was reported.[34]

Especially at reaction temperatures above 200 °C, the Ni_2FeGa performance falls short of the $Cu/ZnO/Al_2O_3/MgO$, which is due to the lower activity of Ni_2FeGa and poisoning through coking at higher temperatures. On repetition of the catalytic test, the Ni_2FeGa had lost almost half its activity after being heated to 250 °C in reaction conditions. It could easily be regenerated through reduction in H_2 producing methane and methanol in the process. This is shown in Figure S7–8 in the supplementary. Long-term stability test of Ni_2FeGa/SiO_2, in Figure S8 right, showed an initial decrease in activity over a course of hours before keeping a stable methanol yield and selectivity for 100 hours. Upon reactivation in H_2, the initial activity and selectivity are obtained.

Based on size-distributions from an *ex situ* TEM analysis of the Ni_2FeGa/SiO_2 catalysts reduced at $\geq$550 °C, surface activity has been estimated and found not to be significantly different for these samples, which means that loss in activity due to a higher reduction temperature is mainly due to decrease in surface-area through sintering. This is shown in Figure S10 of the supplementary in terms of size distributions and surface activity versus reduction temperature plots.

In situ investigation into the reduction and thereby the formation of Ni_2FeGa/SiO_2. To understand the properties achieved through reducing at different temperatures and why 550 °C is an optimum, several *in situ* methods were utilized during the reduction of metal-nitrates into the Ni_2FeGa/SiO_2, which are E-TEM, XRD and XANES/EXAFS.

Environmental Transmission Electron Microscopy. Visualization of a fresh non-reduced sample of Ni_2FeGa showed that nanoparticles were very hard to detect until heating the sample to 300 °C. The area illuminated during heating is shown in Figure S11 of supplementary, showing that nanoparticles are not visible at 200 °C. Figure 4 presents HR-TEM images taken at 300 °C and 500 °C alongside size-distributions made for these temperatures. The atomic planes found with HR-TEM show both metallic nanoparticles with close-packed planes of ~2.1 Å agreeing with the *ex situ* XRD, and particles with larger interplanar distances of 2.4 Å and 2.9 Å which could be oxides. Here it has been found that the nanoparticles grew in size from an average of 3.4 nm to 3.8 nm when heating from 300 °C to

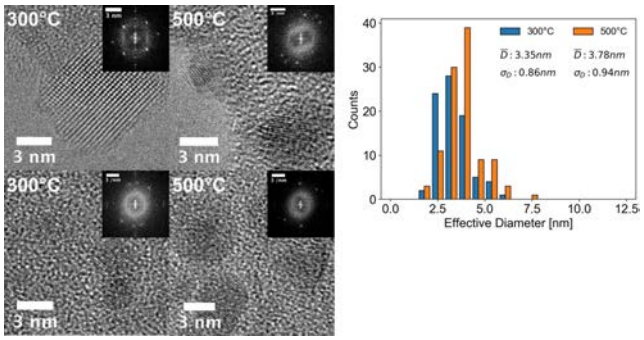

Figure 4. Left, *in situ* HR-TEM images, at 300 °C a large oxide particle with interatomic spacing of 2.4 Å and 2.9 Å, and two small metallic nanoparticles showing ~2.1 Å interatomic spacing. At 500 °C the quantity of the latter having fringes of 2.1 Å has increased. **Right**, size-distribution based on *in situ* TEM images, showing a small increase in the sizes of the nanoparticles at higher temperature.

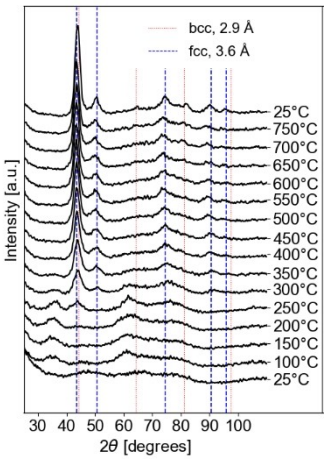

Figure 5. *in situ* XRD of the formation of Ni_2FeGa/SiO_2 a fresh non-reduced sample, while heating the sample in 90 % H_2/He. Lines denote reference-patterns of a face centred cubic lattice and a body centred cubic lattice, with a cubic unit-cell length of 3.6 Å and 2.9 Å. X-ray source was a Cu Kα anode with wavelength 1.5418 Å.

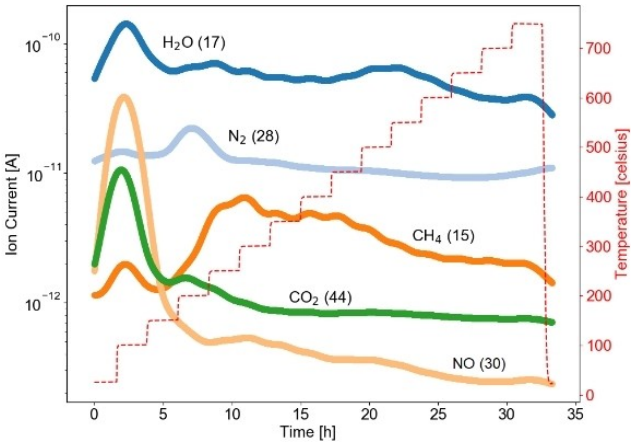

Figure 6. Fourier-filtered Quadrupole Mass-spectroscopy of the outlet gas during in situ XRD. Parentheses denote the detected mass. All detected masses and unfiltered data are shown in Figures S12-14 in the supplementary.

500 °C. During the microscopy, STEM-EDX was performed on individual nanoparticles by parking the beam and acquiring an EDX-spectrum. The quantifications of all the spectra are gathered in Table S3 in the supplementary.

Due to time constraints only 9 individual spectra were acquired which is not nearly statistically significant. Nonetheless comparing STEM-EDX with SEM-EDX of the whole sample stated in Table S4 in the supplementary, show that on average the concentration of iron and gallium is lower than the macroscopic measurement. Thus, if the nanoparticles are representative, the different Ni-species are reduced more than the corresponding Fe- and Ga-species. This corresponds very well to the fact that oxides such as FeO and Ga_2O_3 have a higher formation enthalpy and are harder to reduce compared to NiO.[51,52] This also means that an enlargement of the nanoparticles from 300 °C to 500 °C is not sintering, as this would show on the yield per mass of methanol, but instead the reduction of new species that alloy in the nanoparticles.

In Situ X-ray Diffraction and Quadrupole mass-spectroscopy. Reducing the metal-nitrates into Ni_2FeGa/SiO_2 in H_2 while performing XRD showed large changes of the crystalline structure together with production of various gases measured by Quadrupole mass-spectroscpoy (QMS), both results shown in Figure 5 and 6. From the XRD Figure 5, broad peaks appear at 100–300 °C producing 2θ-peaks at ~35° and ~60°, which can very well be Fe_2O_3 (ICSD cc.: 15840), Fe_3O_4 (ICSD cc.: 26410) or Ga_2O_3 (ICSD cc.: 34243). Metal nitrates decomposing into solid oxides agrees well with the QMS Figure 6, where at 100 °C multiple species are produced being H_2O, NO, and CO_2, and at 200 °C N_2 is produced. H_2O rises again at 250 °C, which correlates with a 2θ-peak at 43° appearing in the XRD pattern. This corresponds very well to an fcc phase of Ni (ICSD cc.: 43397) or Ni_xFe_y (ICSD cc.: 5116, 103555, 103559), especially because the peak intensifies as the temperature rises together with corresponding fcc-peaks appearing at 350 °C. In principle the 2θ-peak at 43° could also be FeO (ICSD cc.: 31081) or NiO (ICSD cc.: 9866) as these would be intermediates before forming metallic nanoparticles but if this is the case, they are very ephemeral. At 550 °C H_2O rises again, very well corresponding to Ga_2O_3 finally being reduced and alloying into the metallic nanoparticles, which is showing as two new 2θ-peaks appearing at 75° and 51° at very low intensity at 650 °C and 750 °C. 2θ-peaks at 44°, 51° and 75° resembles a bcc phase corresponding to the Heusler crystal structure of Ni_2FeGa (ICSD cc.: 157384), though it might not be intermetallic but random in its atomic positions. In conclusion this means that from lower to higher temperatures, the nanoparticles appear to transition from pure Ni into Ni Fe and finally in the ternary alloyed Ni Fe Ga, when the temperature is high enough that Fe and Ga can be reduced. This agrees with the in situ ETEM where it has been concluded that small nanoparticles at low temperatures are containing mostly nickel.

In Situ X-ray Absorption Spectroscopy. The real-space Fourier-transform of the extended fine structure of all the measured edges are shown in Figure 7. The results show for all edges that when heating in H_2, amplitudes from back-scattering on the nearest neighbour elongate from ~1.8 Å to 2 2 Å. Furthermore at well above 200 °C, this structure is still apparent. Since the nitrate-salts will be decomposed at such temperatures as the mass spectroscopy from the in situ XRD shows in Figure 5, this must be scattering from an oxygen neighbour showing that the metals are only partially reduced at lower temperatures. Comparing the different edges it is also obvious that nickel is reduced much more easily than iron and drastically more than gallium, which agrees with the analysis from the *in situ* XRD and ETEM. Linear combination fitting of the XANES using the oxides and the metals at the corresponding edge gave additional insight into the reduction behaviour (Figure S16–19 in the supplementary information). All the edges show intermediate species of oxides when heating from low to high temperatures in agreement with EXAFS and XRD as well.

Fitting of the EXAFS spectra acquired after heating to the highest temperature are shown as dotted lines in Figure 7 and the values for the fitting parameters are presented in Table 2. Looking at the values acquired from the Ni and Fe K-edges, they are almost identical in terms of coordination number, distance and Debye-Waller factor (thermal vibration), thus it is clear that they have a very similar atomic environment. This would certainly be the case if they alloy, though the data do not allow for distinguishing between Ni, Fe and Ga species in the fit. This is probably due to the fact that the sample consists of ternary alloyed nanoparticles, and thus there is not any long-range ordering giving a well-defined coherence in the absorption spectrum. Furthermore the direct back-scattering paths from Ni, Fe and Ga are almost identical, which is exemplified in Figure S20 in the Supplementary. Looking at the Ga K-edge, this element is not fully reduced and alloyed shown by the scattering of an oxygen-atom. Furthermore, the coordination of the Ni/Fe/Ga neighbours is lower meaning that gallium resides more frequently at the surface. The scattering distances from Ga K-edge are equal to the corresponding paths for the Ni and

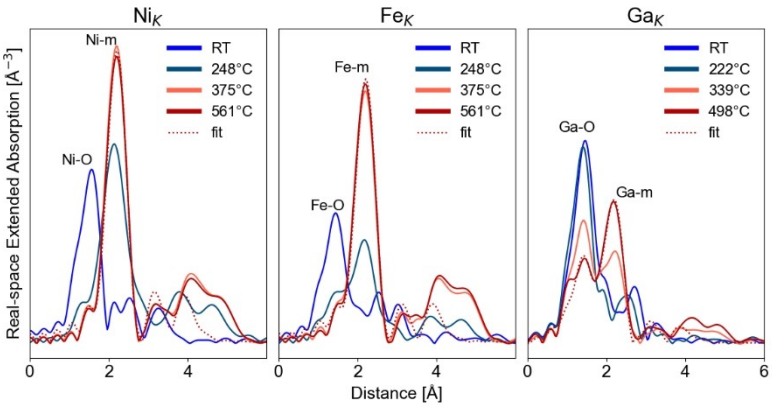

Figure 7. In situ real-space represented k^2-weighted EXAFS of the formation of Ni_2FeGa/SiO_2 from a fresh non-reduced sample. Samples were heated at the denoted temperature in 5 % H_2/He, and subsequently cooled to 50 °C for a proper acquisition of the absorption spectrum. Corresponding XANES are shown in Figure S16 in the supplementary. The dotted lines show fits to data acquired after heating at the highest temperature with parameters given in Table 2. Two separate samples were experimented on, firstly measuring the Ni and Fe K-edges, and subsequently measuring the Ga K-edge.

Table 2. Fitting parameters of Ni_2FeGa after being heated to $\geq$ 500 °C: coordination number N_c, scattering length R, Debye-Waller factor σ. γ-Ni_2FeGa crystal structure was used for fitting the Ni and Fe K-edges, while both γ-Ni_2FeGa and Ga_2O_3 was used for the Ga K-edge.

Edge	Neighbour[b]	N_c	R[a] [Å]	σ[a] [Å]	Residual factor	Fitting range [Å]
Ni K	Ni/Fe/Ga	11.0 ± 1.0	2.52 ± 0.01	0.008 ± 0.001	0.013	1.0 to 4.1
	Ni	4.4 ± 1.3	3.56 ± 0.01	0.012 ± 0.001		
	Ni/Fe/Ga	15 ± 4	4.36 ± 0.01	0.014 ± 0.001		
Fe K	Ni/Ga	12.0[c] ± 1.6	2.51 ± 0.01	0.010 ± 0.001	0.026	1.0 to 4.1
	Fe/Ga	4 ± 2	3.55 ± 0.01	0.014 ± 0.001		
	Ni/Fe	15 ± 6	4.35 ± 0.01	0.018 ± 0.002		
Ga K	O[d]	5.7 ± 0.3	1.81[d] to 1.91[d] ± 0.02	0.006 ± 0.004	0.010	1.1 to 4.0
	Ni/Fe	6.4 ± 0.4	2.51 ± 0.01	0.011 ± 0.001		
	Fe/Ga	2.2 ± 0.5	3.55 ± 0.01	0.016 ± 0.001		
	Ni/Ga	8.2 ± 1.3	4.35 ± 0.01	0.019 ± 0.002		

[a] Change in Scattering-length and Debye-Waller factor have been fitted for each crystal structure, and not for each individual scattering-path. [b] Ni, Fe and Ga species could not be distinguished, as the scattering amplitudes were so correlated that only the sum could be determined by the data. [c] The coordination number has been defined to this value, as the determined value of the amplitude S_0^2 from the reference foil is too low to keep fitting of the coordination number within physical limits. [d] Ga_2O_3 has two non-equivalent positioned gallium-atoms within its unit-cell, meaning that three almost identical scattering paths happen within the first 1.91 Å. These paths have been collectively written in the table as a single O-neighbour of distance 1.81–1.91 Å and the coordination of 5.67 is the sum.

Fe K-edges showing that the reduced gallium has alloyed and a ternary alloy has been achieved after heating to 500 °C.

Conclusion

In this work, Ni Fe Ga supported nanoparticles were synthesised, characterised and tested for their catalytic ability in hydrogenating CO_2. It was found that introducing gallium into Ni Fe nanoparticles tunes the selectivity from producing methane into producing methanol. The binary FeGa without any nickel was unique in its inability to catalyse hydrogenation of CO_2, though no further substantial analysis went into illuminating this property.

The best catalyst in this study was found to be Ni_2FeGa/SiO_2. After optimization of the catalyst preparation, the most active and selective catalyst was found by reducing in H_2 at 550°C for four hours. This final catalyst was compared to a commercial copper-based methanol synthesis catalyst, achieving similar activity at temperatures below 200 °C, but higher temperatures caused the Ni_2FeGa to suffer from lower selectivity and coking.

Comprehensive *in situ* characterisation of the Ni_2FeGa using XRD, TEM and XAS showed how it can alloy from Ni-, Fe- and Ga-nitrate salts. The optimized reduction temperature of 550 °C is exactly the heat-limit at which the Ni_2FeGa is forming in fully ternary metallic nanoparticles, but also cold enough that small nanoparticles are produced increasing the surface area.

Ni_2FeGa/SiO_2 cannot currently out-perform other state-of-the-art catalysts in the field, however, this work shows how the approach of using multiple species with different reduction potential can offer an advantage: producing small alloyed catalytically active nanoparticles.

Experimental Section

Synthesis

The synthesis of SiO_2 supported $Ni_xFe_yGa_z$ nanoparticles was performed using incipient wetness impregnation and subsequent reduction in H_2 at elevated temperatures. Nickel(II)nitrate hexahydrate (10816, Alfa Aesar), iron(III)nitrate nonahydrate (529303, Sigma-Aldrich) and gallium(III)nitrate hydrate (11150, Alfa Aesar) were diluted in Millipore water and impregnated in ground high surface area silica powder (44740, Alfa Aesar) resulting in 16.7 wt% metal loading on SiO_2. Nominal loadings and EDX analysis of composition can be found in Table 1 and Table S1, S2 in the supplementary info. The powder had a grain-size of 105–210 μm. Impregnated silica was subsequently dried for 2 hours at 80 °C in air after which they were loaded in quartz glass-tube reactors to allow a plug-flow and heated using a tube furnace. Here they were reduced in 1.2 bar 90% H_2 in Ar at 800 °C for eight hours before being tested in the same reactor for their catalytic performance.

Pellets of CuO(63.5%)/ZnO(24.7%)/Al_2O_3(10.1%)/MgO(1.3%) (45776, Alfa Aesar) were purchased and ground to a grain-size of 105–210 μm and diluted with SiO_2 (the same material used as the support of $Ni_xFe_yGa_z$). The powder was loaded in a quartz glass-tube reactor and reduced in 1.2 bar 10% H_2 in Ar at 220 °C for 3 hours, then subsequently tested for its catalytic activity. The preparation of the commercial catalyst ensures that CuO is reduced to Cu. The choice of preparation is based on a TPR, shown in Figure S1 in the supplementary. Dilution of the commercial catalyst in SiO_2 was done to achieve equal weight of Cu and $Ni_xFe_yGa_z$ while also having equal geometric dimensions of the reactor-bed. ZnO and MgO are here considered as being support-material of the commercial catalyst.

Catalytic testing

Directly after reducing the catalysts in the plug-flow reactor, the reactor was cooled down to 130 °C and the gas-flow changed to 25% CO_2, 75% H_2 and traces of Ar at 1.2 bar, with a GHSV of 8000 h^{-1} and a GHSV per weight of 130000 $N\,cm^3\,h^{-1}\,g_{NiFeGa}^{-1}$ or $N\,cm^3\,h^{-1}\,g_{Cu}^{-1}$. Exact weights of loaded catalyst are written in Table S1 in the supplementary. The reactor-temperature was changed step-wise up and down twice between 145 °C and 250 °C in 15 °C/step and with 1.5 hours steady-state per step. Gas samples were collected approximately every 15 mins at the reactor-exhaust with a gas chromatograph (Agilent 7890a) mounted with a TCD and FID using separate columns and lines: 80/100 HATESEPQ packed column for moisture removal, 19095P-QO4 capillary column and 19095P-MS6 molecular sieve column on the TCD-line; 19091J-413 capillary column on the FID line. Any gas sample taken close to a temperature-change was discarded.

Characterisation

Transmission electron microscopy (TEM) and spectroscopy. After catalytic tests, samples were loaded on a 300-mesh lacey carbon Au TEM-grid (AGS166A3H, Agar Scientific). Bright-field imaging for nanoparticle size-distributions was performed in ultra-high vacuum on a Tecnai T20 G^2 (FEI) with a LaB_6-thermionic filament operated at 200 keV. Size-distributions (Figure S9) were measured by drawing the outline of each observed nanoparticle, measuring the area and calculating a corresponding circular diameter. High Resolution TEM (HR-TEM) and STEM including energy dispersive X-ray spectroscopy (EDX) and electron energy loss spectroscopy (EELS) was performed in ultra-high vacuum on a Titan E-Cell 80-300ST TEM (FEI) with a FEG operated at 300 keV on two samples of Ni_2FeGa/SiO_2 after reduction and catalytic testing: one reduced at 500 °C and one at 800 °C (Figure S3).

Powder X-ray diffraction (XRD). Samples having undergone catalytic testing were pressed to pellets in steel-casings designed for powder XRD. The XRD was performed on the samples in an Empyrean (Malvern Panalytical) with a $Cu_{K\alpha}$-anode. The diffracted beam was filtered through a monochromator and the sample was spun with 3.75 rotations/min.

Scanning electron microscopy (SEM) and EDX. Powder samples both before and after synthesis and test in the plug-flow reactor were loaded on Aluminium stubs with double carbon-tape. SEM-EDX was performed using a Quanta FEG 200 ESEM (FEI) operated at 20 keV and a 0.1 bar vapour pressure. EDX data was collected using an 80 mm^2 X-Max silicon drift detector (Oxford instruments) with 124 eV energy-resolution. The procedure was to scan the beam well within individual catalytic grains for between 30–60 seconds to gather a converged EDX-spectrum. A minimum of eight spectra were gathered for each individual sample.

Environmental transmission electron microscopy and spectroscopy. Impregnated sample of stoichiometry Ni_2FeGa was ground and diluted in propanol after which it was immediately drop-casted on a Nanochip XT through-hole chip (DENSsolutions), in minimal amount to allow for TEM-transparency. After drying in air the chip was loaded on a DENSsolutions Wildfire heating holder and loaded

into a Titan E-Cell 80-300ST TEM (FEI) with a FEG operated at 300 keV. A continuous flow of H_2 at 1.2 mbar was set and the sample was briefly viewed in TEM-mode and low magnification before heating the sample. The sample was heated chronologically to 200 °C, 300 °C and 500 °C while during BF-TEM. At lowest magnification and a spread beam the sample was briefly investigated in order to find proper spots where the sample was sufficiently transparent. A spot was chosen for imaging when heating and cooling, and all other imaging was conducted on unexposed areas in order to minimise beam damage. HR-TEM and STEM-EDX were performed interchangeably after heating to 300 °C and 500 °C.

In situ X-ray diffraction and quadrupole mass spectrometry (QMS). Impregnated sample of stoichiometry Ni_2FeGa was loaded on a ceramic holder and mounted into a furnace with X-ray transparent beryllium windows (XRK 900, Anton Paar) situated within an X'pert Pro diffractometer (Malvern Panalytical) with a $Cu_{K\alpha}$-anode. The diffracted beam was filtered through a monochromator. A continuous flow of H_2 at 1 bar was set and with a gas velocity matching the synthesis and catalytic tests performed in the plug-flow reactor. The sample was heated to 750 °C in steps of 50 °C and with three diffraction-angle scans at each temperature over 1.7 hours. The gas-exhaust was monitored using QMS supplied by Pfeiffer. In order to filter mass-signals from heating and desorption of surface-condensed water, a high-frequency bandwidth-filter was applied to the QMS data. All raw data, filtering and resulting reduced data is available in Figure S13–15 in the supplementary. The Inorganic Crystal Structure Database (ICSD)[53] has been used for recognizing different crystal structures and ICSD collection codes are noted in parentheses when discussed in the text.

In situ X-ray absorption spectroscopy (XAS). Impregnated sample of stoichiometry Ni_2FeGa was loaded into a 1.5 mm(Ø) capillary with a bed length of 4 mm and a gas-flow of 5 % H_2 in He with pressure equilibrated with the atmospheric conditions. XAS experiments were performed at the CAT-ACT beamline at the synchrotron light facility at Karlsruhe Institute of Technology.[54] Heating was performed with a gas-blower and Eurotherm heat regulator and energy was calibrated from a reference metal foil chosen dependant on the measured edge. Spectra for an analysis of the EXAFS were all acquired at 50 °C after treating the sample at higher temperatures (see below), and quick XANES spectra were acquired while heating the sample. The procedure of the experiment was to heat the sample for a specific duration of time before cooling down to 50 °C and acquiring a spectrum for EXAFS, then subsequently heating the sample again to a higher temperature. Two individual experiments were performed at different times with a modestly varying setup: one for acquiring the Ni and Fe K-edges with a gas-flow of 3 ml/min, and one for acquiring the Ga K-edge with a gas-flow of 50 ml/min. For the Ni and Fe K-edges the sample was heated to 248 °C for 50 mins, 375 °C for 30 mins and 561 °C for 10 mins, all with a heating ramp of 40 °C/min at which XANES of the Ni and Fe K-edges were acquired. For the Ga K-edge the sample was heated to 222 °C for 50 mins, 339 °C for 30 mins and 498 °C for 10 mins, all with a heating ramp of 10 °C/min at which XANES of the Ga K-edge was acquired. This procedure was devised during the experiment based on the time at which the XANES of the Ni K-edge did not change noticeably.

Absorption was in all experiments measured in transmission mode with a reference foil: A Fe-foil for the Fe K-edge, a Ni-foil for the Ni K-edge and a W-foil for the Ga K-edge. Data was calibrated and normalised using Athena[55] and subsequently the EXAFS acquired after heating at the highest temperature were fitted using Artemis.[55] Linear combination fitting has been done and is available in Figure S16–19 in the Supporting Information.

Acknowledgements

The A.P. Møller and Chastine Mc-Kinney Møller Foundation is gratefully acknowledged for the contribution towards the establishment of the Center for Electron Nanoscopy in the Technical University of Denmark. We would like to thank the Institute for Beam Physics and Technology (IBPT) for the operation of the storage ring, the Karlsruhe Research Accelerator (KARA). We acknowledge the KIT light source for provision of instruments at the CAT-ACT beamline of the Institute of Catalysis Research and Technology (IKFT). This work was supported by a research grant (9455) from VILLUM FONDEN. In addition, DanScatt is acknowledged for funding the research stay in Karlsruhe, Germany.

Conflict of Interest

The authors declare no conflict of interest.

Keywords: Methanol synthesis · CO_2 hydrogenation · thermal catalysis · intermetallics · Heusler alloys · ternary alloys · in situ characterization · TEM · XRD · EXAFS

[1] G. A. Olah, A. Goeppert, G. K. S. Prakash, *Angew. Chem. Int. Ed.* **2005**, *44*, 2636–2639; *Angew. Chem.* **2005**, *117*, 2692–2696.
[2] G. A. Olah, A. Goeppert, G. K. S. Prakash, *J. Chem.* **2009**, *2*, 487–498.
[3] G. A. Olah, *Angew. Chem. Int. Ed.* **2013**, *52*, 104–107; *Angew. Chem.* **2013**, *125*, 112–116.
[4] D. W. Keith, *Science* **2009**, *325*, 1654–1656.
[5] G. Bozzano, F. Manenti, *Prog. Energy Combust. Sci.* **2016**, *56*, 71–105.
[6] M. Behrens, F. Studt, I. Kasatkin, S. Kühl, M. Hävecker, F. Abild-Pedersen, S. Zander, F. Girgsdies, P. Kurr, B. Kniep, M. Tovar, R. W. Fischer, J. K. Nørskov, R. Schlögl, *Science* **2012**, *336*, 893–898.
[7] S. Kuld, M. Thorhauge, H. Falsig, C. F. Elkjær, S. Helveg, I. Chorkendorff, J. Sehested, *Science* **2016**, *352*, 969–974.
[8] S. Kuld, C. Conradsen, P. G. Moses, I. Chorkendorff, J. Sehested, *Angew. Chem. Int. Ed.* **2014**, *53*, 5941–5945; *Angew. Chem.* **2014**, *126*, 6051–6055.
[9] F. Studt, M. Behrens, E. L. Kunkes, N. Thomas, S. Zander, *ChemCatChem* **2015**, 1105–1111.
[10] J. T. Sun, I. S. Metcalfe, M. Sahibzada, *Ind. Eng. Chem.* **1999**, *38*, 3868–3872.
[11] M. B. Fichtl, D. Schlereth, N. Jacobsen, I. Kasatkin, J. Schumann, M. Behrens, R. Schlögl, O. Hinrichsen, *Appl. Catal. A* **2015**, *502*, 262–270.
[12] E. L. Kunkes, F. Studt, F. Abild-Pedersen, R. Schlögl, M. Behrens, *J. Catal.* **2015**, *328*, 43–48.
[13] J. Ye, C. Liu, D. Mei, Q. Ge, *ACS Catal.* **2013**, *3*, 1296–1306.
[14] M. Dou, M. Zhang, Y. Chen, Y. Yu, *Comput. Theor. Chem.* **2018**, *1126*, 7–15.
[15] K. Sun, Z. Fan, J. Ye, J. Yan, Q. Ge, Y. Li, W. He, W. Yang, C. Liu, *J. CO2 Util.* **2015**, *12*, 1–6.
[16] O. Martin, A. J. Martín, C. Mondelli, S. Mitchell, T. F. Segawa, R. Hauert, C. Drouilly, D. Curulla-Ferré, J. Pérez-Ramírez, *Angew. Chem. Int. Ed.* **2016**, *55*, 6261–6265; *Angew. Chem.* **2016**, *128*, 6369–6373.
[17] N. Rui, Z. Wang, K. Sun, J. Ye, Q. Ge, C. J. Liu, *Appl. Catal. B* **2017**, *218*, 488–497.
[18] C. Y. Chou, R. F. Lobo, *Appl. Catal. A* **2019**, *583*, 117144.
[19] M. S. Frei, C. Mondelli, R. García-Muelas, K. S. Kley, B. Puértolas, N. López, O. V. Safonova, J. A. Stewart, D. Curulla Ferré, J. Pérez-Ramírez, *Nat. Commun.* **2019**, *10*, 1–11.
[20] T. Fujitani, M. Saito, Y. Kanai, T. Watanabe, J. Nakamura, T. Uchijima, *Appl. Catal. A* **1995**, *125*, L199–L202.
[21] S. Kang, J. Wook, P. S. S. Prasad, J. Oh, K. Jun, S. Song, K. Min, *J. Ind. Eng. Chem.* **2009**, *15*, 665–669.
[22] J. Toyir, D. Piscina, J. Llorca, *Phys. Chem. Chem. Phys.* **2001**, *3*, 4837–4842.

[23] W. Cai, P. Ramirez, D. Piscina, J. Toyir, N. Homs, *Catal. Today* **2015**, *242*, 193–199.
[24] J. C. Medina, M. Figueroa, R. Manrique, J. Rodríguez Pereira, P. D. Srinivasan, J. J. Bravo-Suárez, V. G. Baldovino Medrano, R. Jiménez, A. Karelovic, *Catal. Sci. Technol.* **2017**, *7*, 3375–3387.
[25] A. L. Bonivardi, D. L. Chiavassa, C. A. Querini, M. A. Baltanás, *Stud. Surf. Sci. Catal.* **2000**, *130*, 3747–3752.
[26] E. M. Fiordaliso, I. Sharafutdinov, H. W. P. Carvalho, J.-D. Grunwaldt, T. W. Hansen, I. Chorkendorff, J. B. Wagner, C. D. Damsgaard, *ACS Catal.* **2015**, *5*, 5827–5836.
[27] A. García-Trenco, E. R. White, A. Regoutz, D. J. Payne, M. S. P. Shaffer, C. K. Williams, *ACS Catal.* **2017**, *7*, 1186–1196.
[28] E. M. Fiordaliso, I. Sharafutdinov, H. W. P. Carvalho, J. Kehres, J. D. Grunwaldt, I. Chorkendorff, C. D. Damsgaard, *Sci. Technol. Adv. Mater.* **2019**, *20*, 521–531.
[29] M. Gentzen, D. E. Doronkin, T. L. Sheppard, J. D. Grunwaldt, J. Sauer, S. Behrens, *Appl. Catal. A* **2018**, *562*, 206–214.
[30] M. Gentzen, D. E. Doronkin, T. L. Sheppard, A. Zimina, H. Li, J. Jelic, F. Studt, J. Grunwaldt, J. Sauer, S. Behrens, *Angew. Chem. Int. Ed.* **2019**, *131*, 15802–15806.
[31] C. K. Williams, D. J. Payne, A. García-Trenco, E. R. White, A. Regoutz, M. S. P. Shaffer, *Appl. Catal. B* **2018**, *220*, 9–18.
[32] J. L. Snider, V. Streibel, M. A. Hubert, T. S. Choksi, E. Valle, D. C. Upham, J. Schumann, M. S. Duyar, A. Gallo, F. Abild-Pedersen, T. F. Jaramillo, *ACS Catal.* **2019**, *9*, 3399–3412.
[33] J. A. Singh, A. Cao, J. Schumann, T. Wang, J. K. Nørskov, F. A. Pedersen, S. F. Bent, *Catal. Lett.* **2018**, *148*, 3583–3591.
[34] F. Studt, I. Sharafutdinov, F. Abild-Pedersen, C. F. Elkjær, J. S. Hummelshøj, S. Dahl, I. Chorkendorff, J. K. Nørskov, *Nat. Chem.* **2014**, *6*, 320–324.
[35] I. Sharafutdinov, C. F. Elkjær, H. Wallace, P. De Carvalho, D. Gardini, G. L. Chiarello, C. D. Damsgaard, J. B. Wagner, J. Grunwaldt, S. Dahl, I. Chorkendorff, *J. Catal.* **2014**, *320*, 77–88.
[36] A. Gallo, J. L. Snider, D. Sokaras, D. Nordlund, T. Kroll, H. Ogasawara, L. Kovarik, M. S. Duyar, T. F. Jaramillo, *Appl. Catal. B* **2019**, 118369.
[37] L. C. Grabow, M. Mavrikakis, *ACS Catal.* **2011**, *1*, 365–384.
[38] T. Kojima, S. Kameoka, A. Tsai, *ACS Omega* **2017**, *2*, 147–153.
[39] T. Kojima, S. Kameoka, S. Fujii, S. Ueda, A. Tsai, *Sci. Adv.* **2018**, *4*, 1–8.
[40] F. Heusler, E. Take, *Phys. Z.* **1912**, *13*, 169–184.
[41] C. Felser, H. Atsufumi, *Heusler Alloys*, Springer International Publishing, **2016**.
[42] Y. Xu, M. Liu, X. Huang, Z. Dai, H. Qiu, G. Yu, L. Pan, *Mater. Res. Express* **2016**, *3*, 1–6.
[43] Y. Zhao, L. Wang, X. Hao, J. Wu, *Front. Chem. Eng. China* **2010**, *4*, 153–162.
[44] S. R. Craxford, *Mech. Tech. Synth. Transform. Hydrocarb.* **1939**, *Section A.*, 946–958.
[45] M. A. Vannice, *J. Catal.* **1975**, *37*, 449–461.
[46] M. E. Dry, J. C. Hoogendoorn, *Catal. Rev.* **1981**, *23*, 265–278.
[47] Z. H. Liu, M. Zhang, Y. T. Cui, Y. Q. Zhou, W. H. Wang, G. H. Wu, X. X. Zhang, G. Xiao, *Appl. Phys. Lett.* **2003**, *82*, 424–426.
[48] Z. H. Liu, H. Liu, X. X. Zhang, M. Zhang, X. F. Dai, H. N. Hu, J. L. Chen, G. H. Wu, *Phys. Lett. A* **2004**, *329*, 214–220.
[49] P. J. Brown, A. P. Gandy, K. Ishida, R. Kainuma, T. Kanomata, H. Morito, K. U. Neumann, K. Oikawa, K. R. A. Ziebeck, *J. Phys. Condens. Matter* **2007**, *19*, 016201.
[50] J. F. Qian, H. G. Zhang, J. L. Chen, W. H. Wang, G. H. Wu, *J. Cryst. Growth* **2014**, *388*, 107–111.
[51] J. E. Saal, S. Kirklin, M. Aykol, B. Meredig, C. Wolverton, *JOM* **2013**, *65*, 1501–1509.
[52] S. Kirklin, J. E. Saal, B. Meredig, A. Thompson, J. W. Doak, M. Aykol, S. Rühl, C. Wolverton, *NPJ Comput. Mater.* **2015**, *1*, 15010.
[53] A. Belkly, M. Helderman, V. L. Karen, P. Ulkch, *Acta Crystallogr. Sect. B* **2002**, *58*, 364–369.
[54] A. Zimina, K. Dardenne, M. A. Denecke, D. E. Doronkin, E. Huttel, H. Lichtenberg, S. Mangold, T. Pruessmann, J. Rothe, T. Spangenberg, R. Steininger, T. Vitova, H. Geckeis, J.-D. Grunwaldt, *Rev. Sci. Instrum.* **2017**, *88*, 113113.
[55] B. Ravel, M. Newville, *J. Synchrotron Radiat.* **2005**, *12*, 537–541.